# Chirality Reversal with the Carrier-Envelope Phase: A Next Generation QTAIM Interpretation

**Xinjie Zhou[1], Huan He[1], Genwei Hong[1], Xiao Peng Mi[1], Tianlv Xu[1], Herbert Früchtl[2], Tanja van Mourik[2], Martin, J. Paterson[3], Steven R. Kirk[*1] and Samantha Jenkins[*1]**

*[1]Key Laboratory of Chemical Biology and Traditional Chinese Medicine Research and Key Laboratory of Resource National and Local Joint Engineering Laboratory for New Petro-chemical Materials and Fine Utilization of Resources, College of Chemistry and Chemical Engineering, Hunan Normal University, Changsha, Hunan 410081, China*

*[2]EaStCHEM School of Chemistry, University of Saint Andrews, North Haugh, St Andrews, Fife KY16 9ST, Scotland, United Kingdom.*

*[3]Institute of Chemical Sciences, School of Engineering and Physical Sciences, Heriot-Watt University, Edinburgh, EH14 4AS, UK*

email: steven.kirk@cantab.net
email: samanthajsuman@gmail.com

Simulated circularly-polarized 10 femtosecond laser pulses that induce a mixture of excited states are applied to ethane. Additionally, the carrier-envelope phase (CEP) angle $\phi$, that quantifies the relationship between the time-varying direction of electric (**E**)-field and the amplitude envelope was used to manipulate the mechanical and chiral properties of ethane using Next Generation Quantum Theory of Atoms in Molecules (NG-QTAIM). The chirality assignments were reversed from **S** to **R** as the CEP angle $\phi$ was increased from $\phi = 0.0°$ to $\phi = 180°$. A one-to-one mapping between the CEP angle $\phi$ and NG-QTAIM trajectories was discovered.

## 1. Introduction

The carrier-envelope phase (CEP) angle $\phi$ of a laser pulse is defined as the phase difference $\phi$ between the time-dependent phases of the laser pulse 'envelope', i.e. the time-dependent *scalar* magnitude of the electric (**E**)-field and the time dependent *direction* vector of the electric (**E**)-field associated with the carrier wave, at a reference time. This reference time is usually taken as being the time of peak magnitude of the pulse, however in this investigation we use only circularly polarized pulses and adopt the alternate convention of the reference time being the start time of the pulse, see the Computational Details section. The variation of the CEP angle $\phi$ provides a method to control the time evolution of the wavefunction $\boldsymbol{\psi}(\mathbf{r})$. The CEP angle $\phi$ has previously been discovered to play a major role in the electron dynamics of processes such as photoelectron emission [1], high-order harmonics generation [2], electron localization [3] and control of electron momentum density [4], when the pulse duration contains only a few optical cycles of the carrier frequency. Since the CEP angle $\phi$ involves a direction vector of the associated laser electric (**E**)-field then the subsequent theoretical analysis should use a *vector*-based quantum chemical theory as opposed to *scalar*-based quantum chemical theory. The goal of this investigation of the effect of varying the CEP angle $\phi$ is to learn more about the relationship $\rho(\mathbf{r}) \rightarrow \boldsymbol{\psi}(\mathbf{r})$ where the inverse mapping $\boldsymbol{\psi}(\mathbf{r}) \rightarrow \rho(\mathbf{r})$ is already understood[5,6] via the use of scalar quantum chemical theory.

For this investigation, next generation QTAIM (NG-QTAIM)[7,8], the vector-based version of the original QTAIM theory [9], will be used to quantify the effect of varying the CEP angle $\phi$. A modest **E**-field strength value will be used to explore the manipulation of electronic chirality as opposed to geometric based chirality, within the NG-QTAIM interpretation.

Ultra-fast laser pulses, applied to a molecule, will, in general, create a superposition of excited states in which the electronic wavefunction evolves on ultra-fast timescales in response to the rapidly changing, in both magnitude and direction, **E**-field associated with the laser pulses. Selective strategies for controlled creation of superpositions of excited states are still an active topic in the research literature, e.g. 'undertuning' and 'overtuning' strategies have had only partial success [10]: it is, however, now experimentally feasible to realize laser-induced selective alignment of molecules relative to fields [11,12].

The relationship between steric and electronic factors was recently discovered to be more complex[13] than previously understood, a fact discernable from inspection of molecular structures for the helical electronic transitions of spiroconjugated molecules[14,15]. Earlier investigations discovered that the NG-QTAIM chirality of glycine and also alanine could be reversed by the application of a linear, static **E**-field[16,17].

Ethane was recently used in investigations of mechanical and chiral properties[18] using NG-QTAIM as well as the interpretation of an achiral molecule using third generation NG-QTAIM. Another recent investigation introduced the use of probes of the NG-QTAIM properties[19]. These recent investigations all used electron dynamics generated by a pair of simulated clockwise (CW, [+1]), right-handed (**R**) and counter-clockwise (CCW,

[-1]), left-handed (**S**) circularly polarized non-ionizing ultra-fast laser pulses. These in turn were used to construct the NG-QTAIM eigenvector trajectories, in place of bond torsions that were used earlier [20].

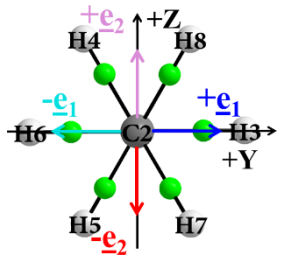


**Scheme 1.** The molecular graph of ethane indicating the *yz* plane, for the pair of applied circularly polarized ultra-fast laser pulses. Clockwise (CW, [+1]), right-handed (**R**) and counter-clockwise (CCW, [-1]), left-handed (**S**) pulses with peak electric (**E**)-field strength, **E** = $5.0\text{x}10^{-4}$ a.u, $10.0\text{x}10^{-4}$ a.u and $200.0\text{x}10^{-4}$ a.u and carrier-envelope phase angles $\phi$ = 0.0°, 30°, 60°, 90°, 120°, 150°, 180° are used, see the Computational Details section. The most ($\pm\underline{\mathbf{e}}_2$) and least ($\pm\underline{\mathbf{e}}_1$) preferred eigenvector directions of the total charge density accumulation $\rho(\mathbf{r}_b)$ at the C1-C2 bond critical point (*BCP*) are shown. Other BCPs are represented by the undecorated green spheres.

In this investigation we will use a pair of simulated clockwise (CW, [+1]), right-handed (**R**) and counter-clockwise (CCW, [-1]), left-handed (**S**) circularly polarized laser pulses for the *yz* plane with CEP angles $\phi$ = 0.0°, 30°, 60°, 90°, 120°, 150°, 180°, to quantify any dependency of the mechanical and chiral properties on the CEP angle $\phi$ as determined by NG-QTAIM, see **Scheme 1**.

## 2. Theoretical Background

The necessary background of QTAIM and next generation QTAIM (NG-QTAIM)[21–27] is provided in the **Supplementary Materials S1**, including the procedure to generate the Hessian of $\rho(\mathbf{r})$ eigenvector-*following* trajectories $\mathbb{T}_{\mathbf{F}}(s)$ and the $\mathbb{U}$-space distortion set $\{\mathbb{F},\mathbb{C},\mathbb{A}\}$. Note the use of the subscript "$_{\mathbf{F}}$" to denote eigenvector-following trajectories $\mathbb{T}_{\mathbf{F}}(s)$ which are created using laser irradiation and not bond torsions as was the case for second-generation trajectories.

The ellipticity, ε, defined as $\varepsilon = |\lambda_1|/|\lambda_2| - 1$, quantifies the relative accumulation of the electronic charge density $\rho(\mathbf{r}_b)$ distribution in the two directions $\pm\underline{\mathbf{e}}_1$ and $\pm\underline{\mathbf{e}}_2$ which are perpendicular to the bond-path at a Bond Critical Point (*BCP*) with position $\mathbf{r}_b$, see **Scheme 1**. For ellipticity $\varepsilon > 0$, the shortest and longest axes of the elliptical distribution of $\rho(\mathbf{r}_b)$ are associated with the $\lambda_1$ and $\lambda_2$ eigenvalues, respectively. From the electron-preceding perspective a change in the electronic charge density $\rho(\mathbf{r})$ distribution that defines a chemical bond causes a change in atomic positions[28]. Bone and Bader later proposed that the direction of motion of the atoms that results from a slightly perturbed structure coincides with the direction of motion of the electrons[29]; this was later confirmed[30,31].

The $\pm\underline{\mathbf{e}}_1$ and $\pm\underline{\mathbf{e}}_2$ eigenvectors of the Hessian of $\rho(\mathbf{r})$ lie in the *yz* plane of polarization, see **Scheme 1**. Note that the $\pm\mathbf{e}_2$ eigenvector corresponds to the direction in which the electrons at the *BCP* are subject to the most compressive forces[32], therefore $\pm\mathbf{e}_2$ corresponds to the most *facile*, i.e. easier, *direction* for displacement of the *BCP* electrons when the *BCP* is torsioned. Conversely the $\pm\mathbf{e}_1$ corresponds to the directions associated with the least compressive forces. The $\pm\mathbf{e}_3$ eigenvector corresponds to the direction of the tensile forces on the electron density $\rho(\mathbf{r})$ at the *BCP*. The bond-path is defined as the path traced out by the $\pm\underline{\mathbf{e}}_3$ eigenvector of the Hessian of the total charge density $\rho(\mathbf{r})$, passing through the *BCP*, along which $\rho(\mathbf{r})$ is locally maximal with respect to any neighboring paths.

In the $\mathbb{U}$-space distortion set $\{\mathbb{F},\mathbb{C},\mathbb{A}\}$ the bond-flexing $\mathbb{F}$, defined as $\mathbb{F} = [\mathbf{(e_1 \cdot dr)_{max}}]_{CW} - [\mathbf{(e_1 \cdot dr)_{max}}]_{CCW}$, provides a measure of the 'flexing-strain' that a bond-path is under when subjected to an external force such as an **E**-field or a circularly polarized laser pulse.

The bond-chirality $\mathbb{C}$ is defined as the difference in the maximum projections of the dot product of the Hessian of $\rho(\mathbf{r})$ $\mathbf{e}_2$ eigenvector and the *BCP* displacement **dr**, i.e. the $\mathbb{T}_{\mathbf{F}}(s)$ values, between the (CW, [+1], right-handed (**R**)) and (CCW, [-1], left-handed (**S**)) circularly polarized laser pulses: $\mathbb{C} = [\mathbf{(e_2 \cdot dr)_{max}}]_{CW} - [\mathbf{(e_2 \cdot dr)_{max}}]_{CCW}$. The bond-chirality $\mathbb{C}$ quantifies the *circular* displacement of the C1-C2 *BCP* i.e., where the largest magnitude Hessian of $\rho(\mathbf{r})$ eigenvalue ($\lambda_2$) is associated with $\pm\mathbf{e}_2$. The $\pm\mathbf{e}_2$ corresponds to the direction in which the electrons at the *BCP* will be most easily displaced when the *BCP* is subjected to circular displacement i.e. torsion[32]. The signs of the bond-chirality $\mathbb{C}$ and bond-axiality $\mathbb{A}$ determine the dominance of **S** ($\mathbb{C} > 0$, $\mathbb{A} > 0$) or **R** ($\mathbb{C} < 0$, $\mathbb{A} < 0$) character, see **Table 1**. The bond-axiality is defined as $\mathbb{A} = [\mathbf{(e_3 \cdot dr)_{max}}]_{CW} - [\mathbf{(e_3 \cdot dr)_{max}}]_{CCW}$**.** This quantifies the direction of *axial* displacement of the bond critical point (*BCP*) in response to the (CW, [+1], right-handed (**R**)) and (CCW, [-1], left-handed (**S**)) circularly polarized laser pulses, i.e. the sliding of the *BCP* along the bond-path[33]. The chirality-helicity function $\mathbb{C}_{helicity} = \mathbb{C}|\mathbb{A}|$, i.e., the numerical product of the bond-chirality and the magnitude of the bond-axiality $\mathbb{A}$, can be used to determine the nature of any chiral behaviors present in ethane in the presence of a pair of circularly polarized laser pulses. The chirality-helicity function $\mathbb{C}_{helicity}$ will only be used for the *yz* plane of polarization in this investigation. A null-chirality assignment **Q**, defined for values of $\mathbb{C}_{helicity} \approx 0$ was previously discovered for ethane using second-generation eigenvector trajectories[15].

The relationship $\boldsymbol{\psi}(\mathbf{r}) \rightarrow \rho(\mathbf{r})$ will be investigated by quantifying the response of the NG-QTAIM Hessian of $\rho(\mathbf{r})$ trajectories $\mathbb{T}_{\mathbf{F}}(s)$ to the variation of the CEP angle $\phi$, see the yellow and blue cube and sphere markers indicating the end points in **Figure 2**. This investigation is possible since the variation of the CEP angle $\phi$ of the laser pulses provides a method to control the time evolution of the wavefunction $\boldsymbol{\psi}(\mathbf{r})$ and the NG-QTAIM Hessian of $\rho(\mathbf{r})$ trajectories $\mathbb{T}_{\mathbf{F}}(s)$ track the response of the *BCP*, i.e. relating to $\rho(\mathbf{r})$. In particular, we will investigate the

correspondence between the *rotation* in $\mathbb{U}$-space of the positions of the end points of the $\mathbb{T}_{\mathbf{F}}(s)$ as the CEP angle $\phi$ is varied from $\phi = 0.0°$ to 180°.

## 3. Computational Details

The ethane molecule was first geometry-optimized using DFT, with zero applied external electric **E**-field. Pseudo-CI (configuration interaction) singles eigenvectors were subsequently constructed using a set of configuration state functions in the zero external electric (**E**)-field case, using the hybrid linear response time-dependent density functional theory/configuration interaction (LR-TDDFT/CI) approach described in detail in previous literature [34–36]. Both the geometry optimization and TD-DFT calculations were carried out at the CAM-B3LYP[37] /aug-cc-pVTZ[38,39] level. The combination of this choice of functional and this basis set have been shown elsewhere in the literature[40] to provide an accurate description of excited states. The geometry optimization and computation of the fifty lowest-energy excited states were performed using the Gaussian G09 v.E.01[41] package with an 'ultrafine' integration grid and no symmetry constraints. Each time-independent many-electron state was constructed as a linear combination of singly-excited configuration state functions from the TD-DFT calculation. Using the time-dependent CI implementation as implemented in the detCI module[34,35] within the ORBKIT[42] package, a 'dipole moment library' of transition dipole moments between states was precomputed, to be used later within the time-dependent electron dynamics calculation. The electron dynamics were then propagated using the 'clamped nuclei' approximation, with the wavefunction $\boldsymbol{\psi}(\mathbf{r})$ being propagated as a linear complex-weighted sum of the previously computed pseudo-CI singles states, as described previously [34,35]. The propagation of the time-dependent electron dynamics used the many-electron time dependent Schrödinger equation using the field-free Hamiltonian, with an extra semi-classical dipole interaction approximation term $-\boldsymbol{\mu}.\mathbf{E}(t)$, where the dot indicates a vector dot product, $\boldsymbol{\mu}$ is the dipole operator and $\mathbf{E}(t)$ is the time-dependent applied electric field vector. The 'dipole moment library' was thus employed at each dynamics time-step during propagation to calculate the dipole interaction term $-\boldsymbol{\mu}.\mathbf{E}(t)$ and the electron dynamics were propagated for a total of 25 fs using the 'interaction' representation.

From the start of the electron dynamics calculation corresponding to $t = 0$ fs onwards, an external time-dependent electric field vector $\mathbf{E}(t)$ was imposed in the form of a single 10 fs duration 'sine-squared'-shaped circularly-polarized laser pulse with peak amplitude $200 \times 10^{-4}$ a.u. This circularly polarized laser pulse was simulated using time-dependent electric field components $[\mathbf{E}_y(t), \mathbf{E}_z(t)]$ in the *yz* polarization plane, see the molecular coordinate axes as defined in **Scheme 1**. The overall field vector $[\mathbf{E}_y(t), \mathbf{E}_z(t)]$ was computed as the product of the following three terms:

**1.** The 'carrier' wave, commencing at time $t$ = 0 fs with initial phase set to the desired CEP angle $\phi$, taken as the vector [sin($\omega t + \phi$), sin($\omega t + \phi + \pi/2$) ] in the (***y***,***z***) polarization plane, with the selected laser excitation frequency $\omega$.

**2.** An 'envelope' of amplitude corresponding to a single pulse as a half-cycle 'sine-squared' function $\mathbf{E}_{peak}$ $\sin^2(\omega_{env}t)$, also commencing at time $t$ = 0 with phase = 0°, with peak field amplitude $\mathbf{E}_{peak}$ = 200x$10^{-4}$ a.u., with $\omega_{env}$ selected appropriately to give a half-cycle, i.e. single pulse, duration of 10 fs.

**3.** A 'polarization' factor of +1 or -1, applied uniquely to the $\mathbf{E}_z(t)$ field component. This yielded an electric field vector which turned either clockwise (CW, [+1]) and right-handed (**R**), or counter-clockwise (CCW, [-1]) and left-handed (**S**) in the (***y***,***z***) polarization plane, depending on the chosen 'polarization' factor, with increasing time *t*.

The time-dependent CI dynamics calculation then evaluated the instantaneous electric **E**-field components at any given dynamics timestep by cubic-spline interpolation into a lookup table of field components pre-generated at 1001 equally-spaced times from $t$ = 0 fs to $t$ = 10 fs.

An 'energetic broadening' approach to creation of the time-evolving superposition of excited states was used: in the special case of a '$\sin^2$' amplitude envelope function pulse of duration $\Delta$T the energetic 'broadening' created by the field is $\Delta E = \hbar/\Delta T$. Low-lying excited electronic states are usually energetically well-separated, so only very short pulses, like the 10 fs pulse used here, are broad enough to create the desired superposition of excited states. Short pulses are energetically broad, but they are also therefore unselective. A carrier frequency (excitation energy) of $\omega$ = 0.350 a.u. for the laser pulse was thus selected so as to cover a relatively wide range of the lower-lying excited states.

The electron dynamics was propagated using a dynamics timestep of 2.1597x$10^{-4}$ fs, chosen to correspond to exactly 320 dynamics timesteps per cycle of the chosen laser carrier frequency (excitation energy) $\omega$ = 0.350 a.u. Every 20 dynamics timesteps, populations describing the content of the superposition state were recorded. These computed populations were confirmed to preserve overall normalization throughout the entire dynamics simulation, with a maximum deviation of 0.25%. The total charge density distribution $\rho(\mathbf{r})$ was calculated using the first-order reduced density matrix (1RDM), being written to storage as files every 4 dynamics timesteps, in the form of 'snapshots' generated in a 'gridded' scalar field file format, using a grid edge 'padding' distance of 4.0 a.u. on all sides of the molecule and a grid spacing of 0.1 a.u.

Dynamics runs were performed for values of the CEP angle $\phi$ = 0°, 30°, 60°, 90°, 120°, 150° and 180°. A 'timeslice' was then defined within each dynamics run, corresponding to two full cycles of the laser excitation carrier frequency, 'centered' on $t$ = 5 fs i.e., from just before to just after the time corresponding to the peak magnitude of the electric field associated with the laser pulse. The bond critical points (*BCP*s), bond paths and eigenvectors of the Hessian of the density $\rho(\mathbf{r})$ were obtained from the 'gridded' charge density 'snapshots' using the CRITIC2 code[43] with the 'density-smoothing'[44] option, while ensuring that the Poincaré-Hopf relationship was

consistently satisfied. NG-QTAIM properties were obtained using the in-house QuantVec[45] suite which has been written to be compatible with CRITIC2 outputs. For each 'timeslice', eigenvector-following NG-QTAIM trajectories were then calculated.

## 4. Results and discussions

The tabulated excitation energies (frequencies) and the corresponding populations for a carrier excitation frequency $\omega$ = 0.350 a.u. for the *yz* plane of circular laser pulse polarization are provided in the **Supplementary Materials S2** and the **Supplementary Materials S3** respectively. Each selected time slice corresponds to two full cycles of the carrier excitation frequency $\omega$. The (CW, [+1], right-handed (**R**)) and (CCW, [-1], left-handed (**S**)) circularly polarized laser pulse plots are found to be indistinguishable. The mix of electronic states comprises significant populations of the |4>, |6>, |7>, |9> and |12> excited states for a peak **E**-field value **E** = 200.0 x $10^{-4}$ a.u where no significant differences with variation of the CEP angle $\phi$ are present. Additional populations of the multi-reference superposition states for electric **E**-field values of **E** = 5.0 x $10^{-4}$ a.u and **E** = 10.0 x $10^{-4}$ a.u are provided in the **Supplementary Materials S4**.

The ellipticity ε variations of the ethane C1-C2 *BCP* with time (femtoseconds) for the (CW, [+1], right-handed (**R**)) and (CCW, [-1], left-handed (**S**)) circularly polarized laser pulse, in the *yz* plane, for a selection of carrier-envelope phase (CEP) values are presented in **Figures 1**, also see **Scheme 1**. The variation of the ethane C1-C2 *BCP* ellipticity ε with time, for the peak **E**-field can be used to provide a visualization of the effect of varying the CEP angle $\phi$. This can be seen from the shift to the left, along the x-axis (time), of the black arrow that tracks the specific feature of the fourth minimum in the ellipticity ε that occurs for $\phi$ = 0.0, see **Figure 1**. Differences between the (CW, [+1], right-handed (**R**)) and (CCW, [-1], left-handed (**S**)) circularly polarized laser pulses are apparent for some, but not all, values of the ellipticity ε with time. This is due to the *partial* symmetry-breaking properties of the ellipticity ε: however, the ellipticity ε does not provide *full* symmetry-breaking [46]. This results in the inability to differentiate the (CW, [+1], right-handed (**R**)) and (CCW, [-1], left-handed (**S**)) circularly polarized laser pulses for the entire duration of the laser pulses.

Full symmetry-breaking requires consideration of the $\pm\underline{\mathbf{e}}_1$, $\pm\underline{\mathbf{e}}_2$ and $\pm\underline{\mathbf{e}}_3$ eigenvectors that is demonstrated with the eigenvector-following trajectories $\mathbb{T}_F(s)$ which are constructed to follow the response to the electron dynamics, see **Table 1** and **Figure 2**.

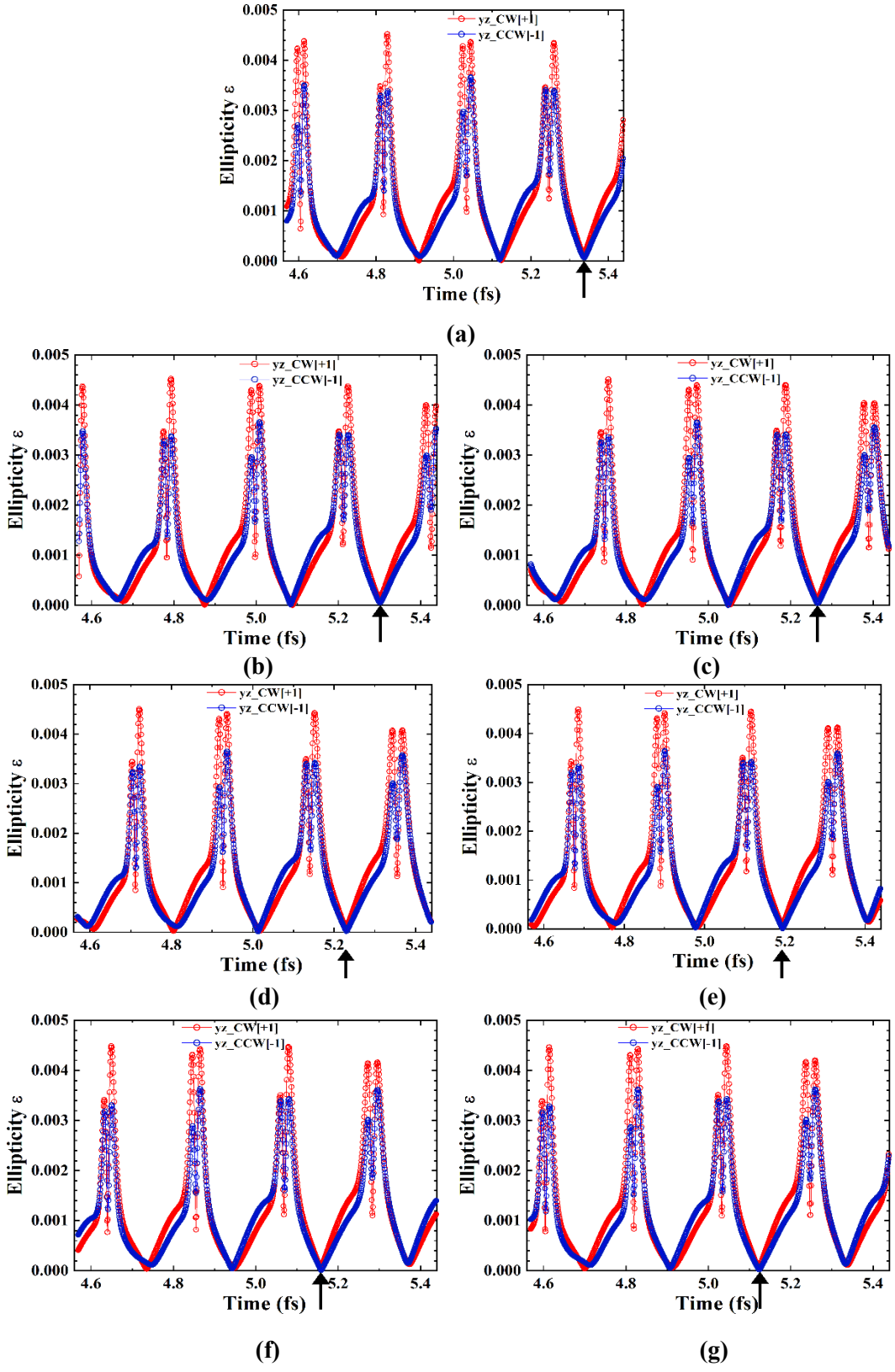


**Figure 1**. The variation of the ethane C1-C2 *BCP* ellipticity ε for the clockwise (**CW[+1]**), right-handed (**R**) and left-handed, counter-clockwise (**CCW[-1]**), left-handed (**S**) circularly polarized laser pulses in the *yz* plane for the carrier-envelope phase (CEP) angle $\phi$ = 0.0°, 30°, 60°, 90°, 120°, 150°, 180° are presented in sub-figures **(a-g)** respectively. Note the position of the black arrow on the axis indicating the effect of varying the CEP angle $\phi$, for further details see **Scheme 1**.

The $\mathbb{T}_{\mathbf{F}}(s)$ trajectories corresponding to the (CW, [+1], right-handed (**R**)) and (CCW, [-1], left-handed (**S**)) circularly polarized laser pulses are separate, unique and distinguishable for the duration of the laser pulses in contrast to the time variations of the ellipticity ε, compare **Figure 2** and **Figure 1**. The intermediate results for (CW, [+1], right-handed (**R**)) and (CCW, [-1], left-handed (**S**)) circularly polarized laser pulses for the peak **E**-field value are provided in the **Supplementary Materials S5**.

The values of the bond-flexing $\mathbb{F}$ varying significantly, up to two orders of magnitude, with variation of the CEP angle $\phi$, with the lowest and highest values for the bond-flexing $\mathbb{F}$ occurring for values of $\phi$ = 30° and $\phi$ = 150° respectively, see **Table 1** and the Theoretical Background section. Correspondingly, large/small values of the chirality $\mathbb{C}$ are present for values of $\phi$ = 30° and $\phi$ = 120°, 150° respectively. The chirality $\mathbb{C}$ assignment changes from **S** to **R** for a value of $\phi$ = 150°: however, the largest value of the bond-flexing $\mathbb{F}$ (-0.0075) corresponds to a value of $\phi$ = 120°, indicating that the **S** to **R** transition starts at $\phi$ = 120°, see **Table 1**. This is consistent with the morphology of the $\mathbb{T}_{\mathbf{F}}(s)$ for $\phi$ = 120° (**Figure 2(e)**) that is intermediate to the morphology of the $\mathbb{T}_{\mathbf{F}}(s)$ for the other values of $\phi$: notice the changing positions of the start and end markers that are denoted by the ball and cube markers respectively, see **Figure 2**. The morphology of the $\mathbb{T}_{\mathbf{F}}(s)$ at $\phi$ = 0° and $\phi$ = 180° are very similar except that the positions of the two sets of start and end markers for the (CW, [+1], right-handed (**R**)) and (CCW, [-1], left-handed (**S**)) $\mathbb{T}_{\mathbf{F}}(s)$ are reversed.

Values of the bond-axiality $\mathbb{A}$ are insignificant for all values of the CEP angle $\phi$, consequently the chirality-helicity function $\mathbb{C}_{helicity} = \mathbb{C}|\mathbb{A}| = 0$.

**Table 1**. The variation of the C1-C2 *BCP* $\mathbb{U}$-space distortion sets $\mathbb{F}$ = bond-flexing$_{max}$, $\mathbb{C}$ = bond-chirality$_{max}$ and $\mathbb{A}$ = bond-axiality$_{max}$} of the C1-C2 *BCPs* of ethane for values of the carrier-envelope phase (CEP) angle $\phi$ = 0.0°, 30°, 60°, 90°, 120°, 150°, 180° for the peak electric field **E** = 200.0 x $10^{-4}$ au in the planes of polarization *yz* are provided; all entries have been multiplied by $10^3$. The corresponding maximum Hessian of $\rho(\mathbf{r})$ eigenvector-following trajectory projections $\mathbb{T}_{\mathbf{F}max}(s)$ for the right-handed **CW (R, [+1])** and left-handed **CCW (S, [-1])** values are provided in the **Supplementary Materials S5**.

| $\phi$ | {$\mathbb{F}$, $\mathbb{C}$, $\mathbb{A}$} |
|---|---|
| 0.0° | { 0.00329274, 0.00257559[**S**], 0.00000230} |
| 30° | { 0.00004961, 0.00003213[**S**], -0.00000547} |
| 60° | { 0.00007895, 0.00004839[**S**], 0.00000070} |
| 90° | { 0.00046799, 0.00021796[**S**], -0.00000223} |
| 120° | {-0.00746819, 0.00371265[**S**], -0.00000568} |
| 150° | { 0.01027771, -0.00242851[**R**], -0.00000495} |
| 180° | {-0.00249622, -0.00205949[**R**], -0.00000244} |

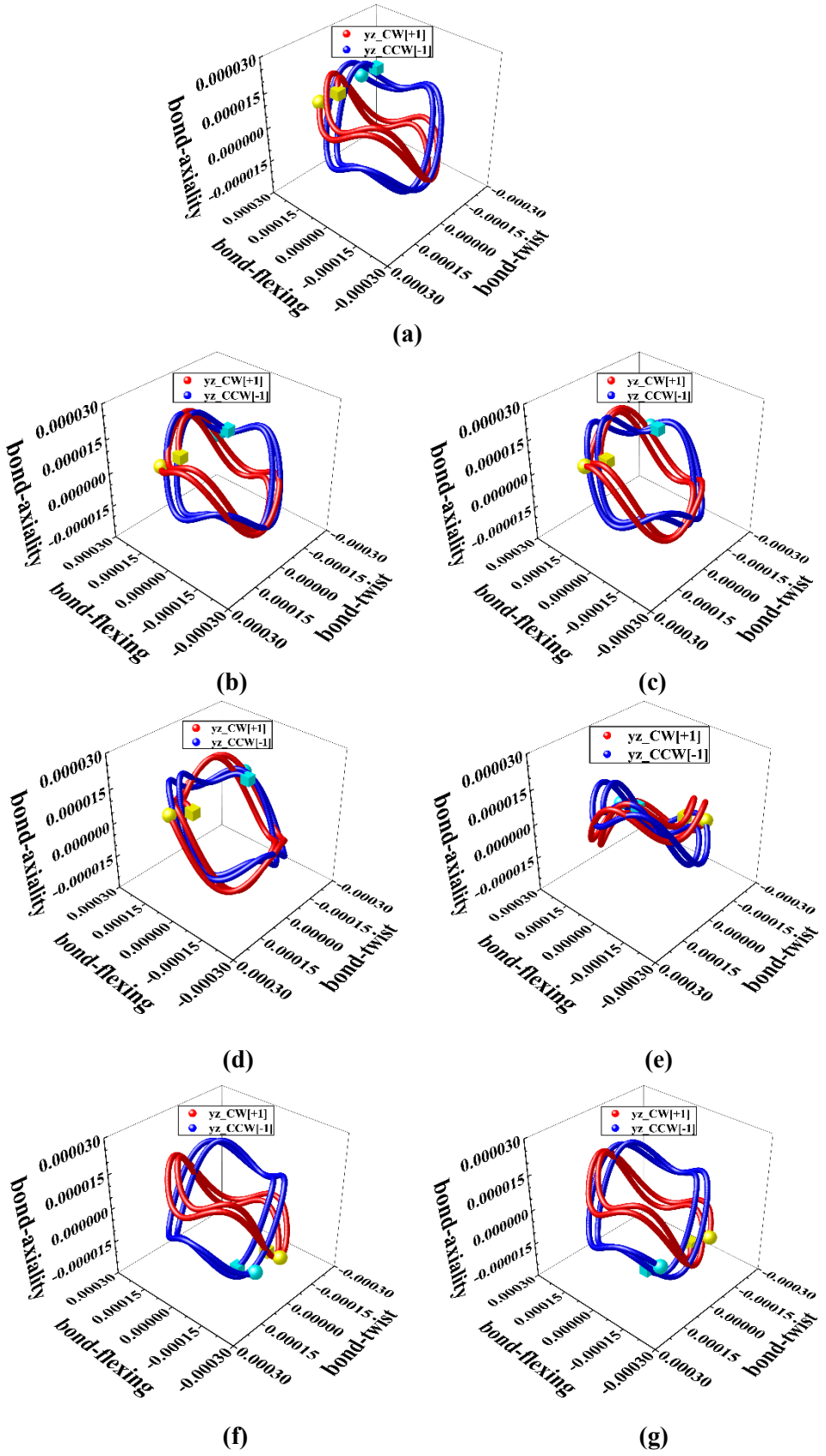


**Figure 2.** The ethane C1-C2 *BCP* Hessian of $\rho(\mathbf{r})$ eigenvector-following trajectories $\mathbb{T}_{\mathbf{F}}(s)$ for the right-handed, clockwise (**CW[+1]**) and left-handed, counter-clockwise (**CCW[-1]**) circularly polarized laser pulses in the *yz* plane for the carrier-envelope phase angle $\phi$ = 0.0°, 30°, 60°, 90°, 120°, 150°, 180° corresponding to the peak electric field **E** = 200.0 x $10^{-4}$ a.u. are presented in sub-figures **(a-g)** respectively. The start and end of each $\mathbb{T}_{\mathbf{F}}(s)$ are denoted by balls and cubes respectively.

## 5. Conclusions

In this investigation we have used NG-QTAIM to quantify the response to varying the CEP angle $\phi$ associated with the simulated electron dynamics of a pair of ultra-fast non-ionizing left- and right-circularly polarized laser pulses of duration 10 femtoseconds that induced a mixture of excited states. In particular, changes to the mechanical (bond-flexing $\mathbb{F}$) and chiral (chirality $\mathbb{C}$) properties were quantified using third generation eigenvector-following trajectories $\mathbb{T}_{\mathbf{F}}(s)$ to generate the $\mathbb{U}$-space distortion set $\{\mathbb{F},\mathbb{C},\mathbb{A}\}$. The outcome of this investigation was that we addressed the goal of learning more about the relationship $\rho(\mathbf{r}) \rightarrow \boldsymbol{\psi}(\mathbf{r})$. This was achieved since the $\mathbb{T}_{\mathbf{F}}(s)$, derived from $\rho(\mathbf{r})$, were used to quantify the effects of varying the circularly polarized laser pulse CEP angle $\phi$ which was in turn used to control the time evolution of the wavefunction $\boldsymbol{\psi}(\mathbf{r})$. In particular, we learned that the effect of varying the CEP angle $\phi$ from $\phi = 0.0°$ to 180° was the reversal of both the chirality (**S** to **R**) assignments and the corresponding $\mathbb{T}_{\mathbf{F}}(s)$ morphologies, i.e. the start and end points of the $\mathbb{T}_{\mathbf{F}}(s)$. This finding also indicated that the $\mathbb{T}_{\mathbf{F}}(s)$ rotated 180° as a consequence of varying the CEP angle $\phi$ from $\phi = 0.0°$ to 180°, therefore quantifying a one-to-one relationship between $\rho(\mathbf{r})$ from the NG-QTAIM $\mathbb{T}_{\mathbf{F}}(s)$ and the time evolution of $\boldsymbol{\psi}(\mathbf{r})$ from the CEP angle $\phi$.

The chirality $\mathbb{C}$ assignment reversal from **S** to **R** occurred for a value of the CEP angle $\phi = 150°$, where the bond-flexing $\mathbb{F}$ had a maximum value for $\phi = 120°$ corresponding to an intermediate morphology of the $\mathbb{T}_{\mathbf{F}}(s)$ indicating the origin of the **S** to **R** chirality $\mathbb{C}$ transition. This is in contrast to our earlier NG-QTAIM investigations using linear, static **E**-fields without the consideration of the CEP angle $\phi$, that were able to reverse the (**S** to **R**) assignments but not the corresponding $\mathbb{T}_{\mathbf{F}}(s)$ morphologies.[16,17]. This inability to reverse the morphology of the $\mathbb{T}_{\mathbf{F}}(s)$ for glycine was due to the asymmetric changes to the $\rho(\mathbf{r})$ distribution induced by the application of the linear, static **E**-field directed parallel or anti-parallel to the bond-path. For alanine the morphologies of the $\mathbb{T}_{\mathbf{F}}(s)$ of the **S** and **R** stereoisomers created by the reversal of the static linear **E**-field were identical were not able to reverse the $\mathbb{T}_{\mathbf{F}}(s)$ morphologies, i.e. the positions of the start and end points of the $\mathbb{T}_{\mathbf{F}}(s)$.

In all cases during the application of the laser pulses, the value of the bond-chirality $\mathbb{C}$ dominates over the bond-axiality $\mathbb{A}$ in agreement with all previous work on ethane with second- and third-generation eigenvector-trajectories. This finding again demonstrates the dominance of steric effects ($\mathbb{C}$) over hyperconjugation ($\mathbb{A}$) in ethane using the NG-QTAIM interpretation. The chirality-helicity function $\mathbb{C}_{helicity} = 0$ for all times during the application of the laser pulses is consistent with the expectations for ethane being a geometrically achiral molecule. Future planned work includes further consideration of the relationship $\rho(\mathbf{r}) \rightarrow \boldsymbol{\psi}(\mathbf{r})$ using the time variation of the

CEP angle $\phi$ of simulated pairs of circularly polarized non-ionizing ultra-fast laser pulses for the investigation of superconductivity. These investigations will use NG-QTAIM to capture the orders of magnitude faster time scales of the response of $\rho(\mathbf{r})$, compared to that of motion of nuclei and hence phonons, that underpin much of the conventional theoretical analysis of superconductivity in the form of e.g. BCS theory whose ongoing use is controversial[47].

**Conflict of Interests Statement**

The authors have no conflict of interests to declare.

**Funding Information**

The Hunan Natural Science Foundation of China project gratefully acknowledged approval number: 2022JJ30029. The One Hundred Talents Foundation of Hunan Province is also gratefully acknowledged for the support of S.J. and S.R.K. MJP thanks the EPSRC for funding through grants EP/T021675 and EP/V006746. The use of SHARCNET computing facilities is acknowledged through the auspices of our sponsor Paul W. Ayers.

**References**

[1] D. Dey, D. Ray, A.K. Tiwari, Controlling Electron Dynamics with Carrier-Envelope Phases of a Laser Pulse, J. Phys. Chem. A 123 (2019) 4702–4707. https://doi.org/10.1021/acs.jpca.9b02870.
[2] N. Ishii, K. Kaneshima, K. Kitano, T. Kanai, S. Watanabe, J. Itatani, Carrier-envelope phase-dependent high harmonic generation in the water window using few-cycle infrared pulses, Nat Commun 5 (2014) 3331. https://doi.org/10.1038/ncomms4331.
[3] P. Lan, E.J. Takahashi, K. Liu, Y. Fu, K. Midorikawa, Carrier envelope phase dependence of electron localization in the multicycle regime, New J. Phys. 15 (2013) 063023. https://doi.org/10.1088/1367-2630/15/6/063023.
[4] C. Lefebvre, D. Gagnon, F. Fillion-Gourdeau, S. MacLean, Carrier-envelope phase effects in graphene, J. Opt. Soc. Am. B, JOSAB 35 (2018) 958–966. https://doi.org/10.1364/JOSAB.35.000958.
[5] G. Frenking, The Chemical Bond – an Entrance Door of Chemistry to the Neighboring Sciences and to Philosophy, Isr. J. Chem. 62 (2022) e202100070. https://doi.org/10.1002/ijch.202100070.
[6] M.W. Schmidt, J. Ivanic, K. Ruedenberg, Covalent bonds are created by the drive of electron waves to lower their kinetic energy through expansion, J Chem Phys 140 (2014) 204104. https://doi.org/10.1063/1.4875735.
[7] S.R. Kirk, S. Jenkins, Tools for overcoming reliance on energy-based measures in chemistry: a tutorial review, Chem. Soc. Rev. 52 (2023) 5861–5874. https://doi.org/10.1039/D3CS00350G.
[8] S. Jenkins, S.R. Kirk, Next Generation Quantum Theory of Atoms in Molecules: From Stereochemistry to Photochemistry and Molecular Devices, 1st ed., Springer Nature, Singapore, 2023. https://doi.org/10.1007/978-981-99-0329-0.
[9] R.F.W. Bader, Atoms in Molecules: A Quantum Theory, 1st Paperback Edition, Clarendon Press, Oxford England : New York, 1994.
[10] G. Füchsel, J.C. Tremblay, T. Klamroth, P. Saalfrank, Selective Excitation of Molecule-Surface Vibrations in H2 and D2 Dissociatively Adsorbed on Ru(0001), Israel Journal of Chemistry 52 (2012) 438–451. https://doi.org/10.1002/ijch.201100097.
[11] I. Tutunnikov, E. Gershnabel, S. Gold, I.Sh. Averbukh, Selective Orientation of Chiral Molecules by Laser Fields with Twisted Polarization, J. Phys. Chem. Lett. 9 (2018) 1105–1111. https://doi.org/10.1021/acs.jpclett.7b03416.

[12] I. Tutunnikov, J. Floß, E. Gershnabel, P. Brumer, I.Sh. Averbukh, A.A. Milner, V. Milner, Observation of persistent orientation of chiral molecules by a laser field with twisted polarization, Phys. Rev. A 101 (2020) 10.1016/j.cpc.2013.10.026. https://doi.org/10.1103/PhysRevA.101.021403.
[13] K.C. Harper, M.S. Sigman, Three-Dimensional Correlation of Steric and Electronic Free Energy Relationships Guides Asymmetric Propargylation, Science 333 (2011) 1875–1878. https://doi.org/10.1126/science.1206997.
[14] M.H. Garner, C. Corminboeuf, Helical electronic transitions of spiroconjugated molecules, Chem. Commun. 57 (2021) 6408–6411. https://doi.org/10.1039/D1CC01904J.
[15] H. Xing, A. Azizi, R. Momen, T. Xu, S.R. Kirk, S. Jenkins, Chirality–helicity of cumulenes: A non-scalar charge density derived perspective, Int. J. Quantum Chem. 122 (2022) e26884. https://doi.org/10.1002/qua.26884.
[16] X. Nie, Y. Yang, T. Xu, M. Biczysko, S.R. Kirk, S. Jenkins, The chirality of isotopomers of glycine compared using next-generation QTAIM, Int. J. Quantum Chem. 122 (2022) e26917. https://doi.org/10.1002/qua.26917.
[17] W. Yu, Z. Li, Y. Peng, X. Feng, T. Xu, H. Früchtl, T. van Mourik, S.R. Kirk, S. Jenkins, Controlling Achiral and Chiral Properties with an Electric Field: A Next-Generation QTAIM Interpretation, Symmetry 14 (2022) 2075. https://doi.org/10.3390/sym14102075.
[18] X.P. Mi, H. Lu, T. Xu, H. Früchtl, T. van Mourik, M.J. Paterson, S.R. Kirk, S. Jenkins, Response of the mechanical and chiral character of ethane to ultra-fast laser pulses, Journal of Computational Chemistry 45 (2023) 150–158. https://doi.org/10.1002/jcc.27225.
[19] H. He, X. Peng Mi, X. Zhou, G. Hong, T. Xu, H. Früchtl, T. van Mourik, M.J. Paterson, S.R. Kirk, S. Jenkins, Ultra-fast laser pulses as a probe of electron dynamics: A next generation QTAIM perspective, Chemical Physics Letters 835 (2023) 141018. https://doi.org/10.1016/j.cplett.2023.141018.
[20] Z. Li, T. Xu, H. Früchtl, T. van Mourik, S.R. Kirk, S. Jenkins, Mixed chiral and achiral character in substituted ethane: A next generation QTAIM perspective, Chemical Physics Letters 803 (2022) 139762. https://doi.org/10.1016/j.cplett.2022.139762.
[21] M.X. Hu, T. Xu, R. Momen, A. Azizi, S.R. Kirk, S. Jenkins, The normal modes of vibration of benzene from the trajectories of stress tensor eigenvector projection space, Chem. Phys. Lett. 677 (2017) 156–161. https://doi.org/10.1016/j.cplett.2017.04.017.
[22] W.J. Huang, T. Xu, S.R. Kirk, M. Filatov, S. Jenkins, QTAIM and stress tensor bond-path framework sets for the ground and excited states of fulvene, Chem. Phys. Lett. 713 (2018) 125–131. https://doi.org/10.1016/j.cplett.2018.10.029.
[23] J.H. Li, W.J. Huang, T. Xu, S.R. Kirk, S. Jenkins, Stress Tensor Eigenvector Following with Next-Generation Quantum Theory of Atoms in Molecules, Int. J. Quantum Chem. 119 (2018) e25847. https://doi.org/10.1002/qua.25847.
[24] H. Guo, A. Morales-Bayuelo, T. Xu, R. Momen, L. Wang, P. Yang, S.R. Kirk, S. Jenkins, Distinguishing and quantifying the torquoselectivity in competitive ring-opening reactions using the stress tensor and QTAIM, J. Comput. Chem. 37 (2016) 2722–2733. https://doi.org/10.1002/jcc.24499.
[25] P. Yang, T. Xu, R. Momen, A. Azizi, S.R. Kirk, S. Jenkins, Fatigue and photochromism S1 excited state reactivity of diarylethenes from QTAIM and the stress tensor, Int. J. Quantum Chem. 118 (2018) e25565. https://doi.org/10.1002/qua.25565.
[26] T. Xu, L. Wang, Y. Ping, T. van Mourik, H. Früchtl, S.R. Kirk, S. Jenkins, Quinone-based switches for candidate building blocks of molecular junctions with QTAIM and the stress tensor, Int. J. Quantum Chem. 118 (2018) e25676. https://doi.org/10.1002/qua.25676.
[27] T. Xu, J. Farrell, R. Momen, A. Azizi, S.R. Kirk, S. Jenkins, D.J. Wales, A Stress Tensor Eigenvector Projection Space for the (H2O)5 Potential Energy Surface, Chem. Phys. Lett. 667 (2017) 25–31. https://doi.org/10.1016/j.cplett.2016.11.028.
[28] H. Nakatsuji, Common nature of the electron cloud of a system undergoing change in nuclear configuration, J. Am. Chem. Soc. 96 (1974) 24–30. https://doi.org/10.1021/ja00808a004.
[29] R.G.A. Bone, R.F.W. Bader, Identifying and Analyzing Intermolecular Bonding Interactions in van der Waals Molecules, J. Phys. Chem. 100 (1996) 10892–10911. https://doi.org/10.1021/jp953512m.
[30] S. Jenkins, M.I. Heggie, Quantitative analysis of bonding in 90° partial dislocation in diamond, J. Phys.:

Condens. Matter 12 (2000) 10325–10333. https://doi.org/10.1088/0953-8984/12/49/3.
[31] P.W. Ayers, S. Jenkins, An electron-preceding perspective on the deformation of materials, J. Chem. Phys. 130 (2009) 154104. https://doi.org/10.1063/1.3098140.
[32] P. Szarek, Y. Sueda, A. Tachibana, Electronic stress tensor description of chemical bonds using nonclassical bond order concept, J. Chem. Phys. 129 (2008) 094102. https://doi.org/10.1063/1.2973634.
[33] T. Tian, T. Xu, S.R. Kirk, I.T. Rongde, Y.B. Tan, S. Manzhos, Y. Shigeta, S. Jenkins, Intramolecular Mode Coupling of the Isotopomers of Water: A Non-Scalar Charge Density-Derived Perspective, Phys. Chem. Chem. Phys. 22 (2020) 2509–2520. https://doi.org/10.1039/C9CP05879F.
[34] V. Pohl, G. Hermann, J.C. Tremblay, An open-source framework for analyzing N-electron dynamics. I. Multideterminantal wave functions, Journal of Computational Chemistry 38 (2017) 10.1002/jcc.24896. https://doi.org/10.1002/jcc.24792.
[35] G. Hermann, V. Pohl, J.C. Tremblay, An open-source framework for analyzing N-electron dynamics. II. Hybrid density functional theory/configuration interaction methodology, Journal of Computational Chemistry 38 (2017) 2378–2387. https://doi.org/10.1002/jcc.24896.
[36] S. Giri, A.M. Dudzinski, J.C. Tremblay, G. Dixit, Time-dependent electronic current densities in chiral molecules, Phys. Rev. A 102 (2020) 063103. https://doi.org/10.1103/PhysRevA.102.063103.
[37] T. Yanai, D.P. Tew, N.C. Handy, A new hybrid exchange–correlation functional using the Coulomb-attenuating method (CAM-B3LYP), Chemical Physics Letters 393 (2004) 51–57. https://doi.org/10.1016/j.cplett.2004.06.011.
[38] R.A. Kendall, T.H. Dunning, R.J. Harrison, Electron affinities of the first-row atoms revisited. Systematic basis sets and wave functions, J. Chem. Phys. 96 (1992) 6796–6806. https://doi.org/10.1063/1.462569.
[39] T.H. Dunning, Gaussian basis sets for use in correlated molecular calculations. I. The atoms boron through neon and hydrogen, J. Chem. Phys. 90 (1989) 10.1021/acs.jctc.0c01228. https://doi.org/10.1063/1.456153.
[40] R. Sarkar, M. Boggio-Pasqua, P.-F. Loos, D. Jacquemin, Benchmarking TD-DFT and Wave Function Methods for Oscillator Strengths and Excited-State Dipole Moments, J. Chem. Theory Comput. 17 (2021) 1117–1132. https://doi.org/10.1021/acs.jctc.0c01228.
[41] Michael J. Frisch, G. W. Trucks, H. Bernhard Schlegel, Gustavo E. Scuseria, Michael A. Robb, James R. Cheeseman, Giovanni Scalmani, Vincenzo Barone, Benedetta Mennucci, G. A. Petersson, H. Nakatsuji, M. Caricato, Xiaosong Li, H. P. Hratchian, Artur F. Izmaylov, Julien Bloino, G. Zheng, J. L. Sonnenberg, M. Hada, M. Ehara, K. Toyota, R. Fukuda, J. Hasegawa, M. Ishida, T. Nakajima, Y. Honda, O. Kitao, H. Nakai, T. Vreven, J. A. Montgomery Jr., J. E. Peralta, François Ogliaro, Michael J. Bearpark, Jochen Heyd, E. N. Brothers, K. N. Kudin, V. N. Staroverov, Rika Kobayashi, J. Normand, Krishnan Raghavachari, Alistair P. Rendell, J. C. Burant, S. S. Iyengar, Jacopo Tomasi, M. Cossi, N. Rega, N. J. Millam, M. Klene, J. E. Knox, J.B. Cross, V. Bakken, C. Adamo, J. Jaramillo, R. Gomperts, R.E. Stratmann, O. Yazyev, A.J. Austin, R. Cammi, C. Pomelli, J.W. Ochterski, R.L. Martin, K. Morokuma, V.G. Zakrzewski, G.A. Voth, P. Salvador, J.J. Dannenberg, S. Dapprich, A.D. Daniels, Ö. Farkas, J.B. Foresman, J.V. Ortiz, J. Cioslowski, D.J. Fox, Gaussian 09, Revision E.01, (2009). www.gaussian.com.
[42] G. Hermann, V. Pohl, J.C. Tremblay, B. Paulus, H.-C. Hege, A. Schild, ORBKIT: A modular python toolbox for cross-platform postprocessing of quantum chemical wavefunction data, Journal of Computational Chemistry 37 (2016) 1511–1520. https://doi.org/10.1002/jcc.24358.
[43] A. Otero-de-la-Roza, E.R. Johnson, V. Luaña, Critic2: A program for real-space analysis of quantum chemical interactions in solids, Computer Physics Communications 185 (2014) 1007–1018. https://doi.org/10.1016/j.cpc.2013.10.026.
[44] A. Otero-de-la-Roza, Finding critical points and reconstruction of electron densities on grids, The Journal of Chemical Physics 156 (2022) 224116. https://doi.org/10.1063/5.0090232.
[45] S.R. Kirk, S. Jenkins, QuantVec, (2021). DOI.org/10.5281/zenodo.5553686 (accessed October 7, 2021).
[46] S.R. Kirk, S. Jenkins, Beyond energetic and scalar measures: Next generation quantum theory of atoms in molecules, WIREs Comput. Mol. Sci. 12 (2022) :10.1002/jcc.24358. https://doi.org/10.1002/wcms.1611.
[47] J.E. Hirsch, Superconducting materials: Judge and jury of BCS-electron–phonon theory, Applied Physics Letters 121 (2022) 080501. https://doi.org/10.1063/5.0104968.